



**HAL**  
open science

## The metallicity distribution in the core of the Sagittarus dwarf spheroidal: Minimising the metallicity biases

Alice Minelli, Michele Bellazzini, Alessio Mucciarelli, Piercarlo Bonifacio, Rodrigo Ibata, Donatella Romano, Lorenzo Monaco, Elisabetta Caffau, Emanuele Dalessandro, Raffaele Pascale

### ► To cite this version:

Alice Minelli, Michele Bellazzini, Alessio Mucciarelli, Piercarlo Bonifacio, Rodrigo Ibata, et al.. The metallicity distribution in the core of the Sagittarus dwarf spheroidal: Minimising the metallicity biases. *Astronomy & Astrophysics - A&A*, 2023, 669, 10.1051/0004-6361/202244890 . insu-03932154

**HAL Id: insu-03932154**

**<https://insu.hal.science/insu-03932154v1>**

Submitted on 10 Jan 2023



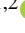






**HAL** is a multi-disciplinary open access archive for the deposit and dissemination of scientific research documents, whether they are published or not. The documents may come from teaching and research institutions in France or abroad, or from public or private research centers.

L'archive ouverte pluridisciplinaire **HAL**, est destinée au dépôt et à la diffusion de documents scientifiques de niveau recherche, publiés ou non, émanant des établissements d'enseignement et de recherche français ou étrangers, des laboratoires publics ou privés.



Distributed under a Creative Commons Attribution 4.0 International License

# The metallicity distribution in the core of the Sagittarius dwarf spheroidal: Minimising the metallicity biases<sup>★,★★</sup>

Alice Minelli<sup>1</sup>, Michele Bellazzini<sup>2</sup>, Alessio Mucciarelli<sup>1,2</sup>, Piercarlo Bonifacio<sup>3</sup>, Rodrigo Ibata<sup>4</sup>,  
Donatella Romano<sup>2</sup>, Lorenzo Monaco<sup>5</sup>, Elisabetta Caffau<sup>3</sup>, Emanuele Dalessandro<sup>2</sup>, and Raffaele Pascale<sup>2</sup>

<sup>1</sup> Dipartimento di Fisica e Astronomia “Augusto Righi”, Alma Mater Studiorum, Università di Bologna, Via Gobetti 93/2, 40129 Bologna, Italy

e-mail: [alice.minelli4@unibo.it](mailto:alice.minelli4@unibo.it)

<sup>2</sup> INAF – Osservatorio di Astrofisica e Scienza dello Spazio di Bologna, Via Gobetti 93/3, 40129 Bologna, Italy

<sup>3</sup> GEPI, Observatoire de Paris, Université PSL, CNRS, 5 Place Jules Janssen, 92190 Meudon, France

<sup>4</sup> Université de Strasbourg, CNRS, Observatoire astronomique de Strasbourg, UMR 7550, 67000 Strasbourg, France

<sup>5</sup> Departamento de Ciencias Físicas, Universidad Andres Bello, Fernandez Concha 700, Las Condes, Santiago, Chile

Received 5 September 2022 / Accepted 8 November 2022

## ABSTRACT

We present the metallicity and radial velocity for 450 bona fide members of the Sagittarius dwarf spheroidal (Sgr dSph) galaxy, measured from high-resolution spectra ( $R \approx 18\,000$ ) obtained with FLAMES at the VLT. The targets were carefully selected (a) to sample the core of the main body of Sgr dSph while avoiding contamination from the central stellar nucleus, and (b) to prevent any bias on the metallicity distribution by selecting targets based on their *Gaia* parallax and proper motions. All the targets selected in this way were confirmed as radial velocity members. We used this sample to derive the first metallicity distribution of the core of Sgr dSph, which is virtually unaffected by metallicity biases. The observed distribution ranges from  $[\text{Fe}/\text{H}] \approx -2.3$  to  $[\text{Fe}/\text{H}] \approx 0.0$ , with a strong, symmetric, and relatively narrow peak around  $[\text{Fe}/\text{H}] \approx -0.5$  and a weak and extended metal-poor tail, in which only  $13.8 \pm 1.9\%$  of the stars have  $[\text{Fe}/\text{H}] < -1.0$ . We confirm previous evidence of correlations between chemical and kinematical properties of stars in the core of Sgr. In our sample, stars with  $[\text{Fe}/\text{H}] \geq -0.6$  display a lower velocity dispersion and a higher rotation amplitude than those with  $[\text{Fe}/\text{H}] < -0.6$ , confirming previous suggestions of disk/halo structure for the progenitor of the system.

**Key words.** stars: abundances – galaxies: evolution – Local Group – galaxies: dwarf – techniques: spectroscopic

## 1. Introduction

The Sagittarius dwarf spheroidal galaxy (Ibata et al. 1994, Sgr dSph, hereafter Sgr, for brevity) is the most obvious example of the ongoing disruption of a dwarf satellite into a large galaxy, the Milky Way (MW). We currently see the remnant of the dwarf galaxy, a large, elongated spheroid with low surface brightness that is mostly composed of unbound stars (hereafter the main body; see e.g., Vasiliev & Belokurov 2020; Ferguson & Strigari 2020; del Pino et al. 2021; Carlberg & Grillmair 2022, and references therein), and the two arms of its tidal streams wrapping around the MW (hereafter the stream; Law & Majewski 2016; Ibata et al. 2020; Antoja et al. 2020; Ramos et al. 2020; Vasiliev et al. 2021, and references therein). The disruption of Sgr contributes to the build-up of the MW halo in terms of dark matter, stars, and globular clusters (see e.g., Majewski et al. 2003; Huxor & Grebel 2015; Hasselquist et al. 2019; Bellazzini et al. 2020). The interaction with the MW appears to have left its imprint on the structure, kinematics, and star formation history of the MW disc (see e.g., Laporte et al. 2019; Ruiz-Lara et al. 2020; Carr et al. 2022).

Vasiliev & Belokurov (2020) estimates that the present-day total mass of the main body is  $M \sim 4 \times 10^8 M_\odot$ , with  $M_\star \sim 1 \times 10^8 M_\odot$  in stars, but several lines of evidence suggest that the original progenitor of the system was significantly more massive, in the range  $10^{10}$ – $10^{11} M_\odot$  (Łokas et al. 2010; Niederste-Ostholt et al. 2012; Gibbons et al. 2017; Dierickx & Loeb 2017; Minelli et al. 2021; Vasiliev et al. 2021). Given the advanced stage of disruption, the chemical abundance information that low-mass stars recorded in their atmospheres since the epoch of their birth, is a key element to reconstruct the characteristics of the progenitor of the system that we observe today. The metallicity gradient within the main body of Sgr (see Vitali et al. 2022, for a recent thorough analysis and references) and along the Sgr stream (Bellazzini et al. 2006; Chou et al. 2007; Monaco et al. 2007; Carlin et al. 2012; de Boer et al. 2014; Gibbons et al. 2017; Yang et al. 2019; Hayes et al. 2020; Ramos et al. 2022) is firmly established, suggesting a complex interplay between the metallicity and kinematics that traces the combination of initial conditions in the progenitor and of the disruption process (Gibbons et al. 2017; Yang et al. 2019; Johnson et al. 2020; Ramos et al. 2022).

Disappointingly enough, in spite of the increasingly detailed view of the chemical composition along the stream as well as in the main body, a robust and unbiased determination of the metallicity distribution function (MDF) of the main body is still lacking. The main body of Sgr lies at low Galactic

\* Full Table 1 is only available at the CDS via anonymous ftp to [cdsarc.cds.unistra.fr](https://cdsarc.cds.unistra.fr) (130.79.128.5) or via <https://cdsarc.cds.unistra.fr/viz-bin/cat/J/A+A/669/A54>

\*\* Based on observations collected at the ESO-VLT under programs 105.20AH.001.

longitude and latitude, therefore the colour-magnitude diagram (CMD) from which candidate members can be selected for spectroscopic follow-up is strongly affected by contamination from foreground stars from the bulge and the thick disc of the MW. The combination of high mean metallicity and distance of Sgr makes it relatively easy to select good candidate members from the red (metal-rich) side of the red giant branch (RGB), introducing an observational bias against metal-poor stars in this way that also affects the most recent and thorough studies (see e.g., [Hasselquist et al. 2021](#), their Appendix C in particular, and also [Johnson et al. 2020](#), and references therein). Furthermore, several abundance analysis studies of the system were focused on the very central region of the galaxy ([Monaco et al. 2005](#); [Bellazzini et al. 2008](#); [Carretta et al. 2010a,b](#); [Alfaro-Cuello et al. 2019, 2020](#); [Mucciarelli et al. 2017](#), hereafter M17), which hosts a complex and composite stellar nucleus whose stellar content is not representative of the main body of Sgr ([Siegel et al. 2007](#); [Alfaro-Cuello et al. 2019](#); M17).

Here we report on the results of an experiment aimed at obtaining a well-sampled MDF of the core of Sgr that is not affected by the metallicity biases described above (see Sect. 2 for further details) and is not contaminated by the population of the nuclear region. The main new factor allowing us to obtain an unbiased MDF is a selection of candidate targets for spectroscopy primarily based on *Gaia* EDR3 ([Gaia Collaboration 2021](#)) parallaxes and, especially, proper motions, as was also done by [Vasiliev & Belokurov \(2020\)](#), [Ferguson & Strigari \(2020\)](#), [del Pino et al. \(2021\)](#), [Carlberg & Grillmair \(2022\)](#) and other authors. This effectively removes the MW contaminants from the CMD, providing a clean sample of high-probability Sgr members over the whole colour/metallicity range spanned by Sgr RGBs, thus avoiding biases against metal-poor stars.

As briefly reminded above, the Sgr system is very extended, also when only the main body is considered ([Vasiliev & Belokurov 2020](#); [Majewski et al. 2003](#)), and a metallicity gradient with distance from the centre of the galaxy is observed at any scale (see e.g., [Bellazzini et al. 1999](#); [Alard 2001](#); [Chou et al. 2007](#); [Majewski et al. 2013](#); [Vitali et al. 2022](#)). This means that while we can now gain a much stronger control on metallicity biases, the MDF will unavoidably depend on the sampled radial range. None of the existing studies can claim to have obtained an MDF that is representative of the entire system, or even of the entire main body. Our case is no exception. Our choice is to focus on the core of the main body, and, in particular, on the most central part of the core, which is not contaminated by the stars of the nuclear star cluster. This central, non-nuclear region is assumed to be less impacted by the ongoing disruption process ([del Pino et al. 2021](#)), and therefore is presumably the best approximation available of the conditions near the centre of the Sgr progenitor (but see Sect. 5.4). Our study should be considered a first step in the mapping of the MDF over the Sgr main body without metallicity biases. In the following, whenever we define our MDF as “unbiased”, we mean that metallicity biases are expected to have been reduced to a minimum, presumably negligible, amount.

We secured high-resolution spectra for 450 Sgr members selected in this way, from which we obtained reliable and precise radial velocity (RV) and metallicity measures, finally obtaining the desired MDF of the core of the Sgr main body. The paper is organised as follows: In Sect. 2 we present the sample and report on the determination of the stellar atmospheric parameters, in Sect. 4 we describe the analysis leading to the measure of individual RV and [Fe/H], and in Sect. 5 we show the newly derived

MDF of Sgr dSph, comparing it with those of other nearby dwarf galaxies and with the predictions of chemical evolution models. We also investigate the correlation between metallicity and kinematics in our sample. Finally, in Sect. 6 we summarise our conclusions.

## 2. Spectroscopic dataset

The rationale of our selection is illustrated in Fig. 1. Figure 1a shows the CMD of a circular region within  $1.0^\circ$  from the centre of Sgr (coinciding with the centre of the massive globular cluster M 54). The innermost  $11.5'$  is excised to minimise the contamination by the compact stellar nucleus ([Bellazzini et al. 2008](#); [Carlberg & Grillmair 2022](#)), according to the 2010 version of the [Harris \(1996\)](#) catalogue, where the tidal radius of M 54 is  $r_t = 9.9'$ , while [Bellazzini et al. \(2008\)](#) reported  $r_t \simeq 10.5'$  as the limiting radius of the metal-rich component of the stellar nucleus. While part of the horizontal branch (at  $G \simeq 18.3$  and  $G_{BP} - G_{RP} < 0.7$ ) and the bright asymptotic giant branch (AGB) sequence of Sgr, bending to the red from  $(G, G_{BP} - G_{RP}) \simeq (14.6, 2.3)$ , are relatively clean, its red clump  $(G, G_{BP} - G_{RP}) \simeq (17.9, 1.3)$  and the RGB, from  $(G, G_{BP} - G_{RP}) \simeq (19.0, 1.0)$  to  $(G, G_{BP} - G_{RP}) \simeq (14.6, 2.3)$ , are strongly contaminated by foreground Galactic stars. The blue side of the RGB, which is expected to host the most metal-poor old stars, is especially affected.

However, Fig. 1b shows how we can remove the vast majority of the contaminating stars (virtually all of them) by selecting only stars (1) with proper motions within  $0.5 \text{ mas yr}^{-1}$  of the systemic proper motion of Sgr, as determined by [Gaia Collaboration \(2018b\)](#), and (2) with parallaxes consistent with  $0.0 \text{ mas}$  within about three times the associated uncertainty. The first criterion selects stars with a motion in the plane of the sky within  $\simeq \pm 60 \text{ km s}^{-1}$  from the systemic motion of Sgr. This range is approximately broader than five times the typical line-of-sight (los) velocity dispersion in the main body ([Bellazzini et al. 2008](#); [Majewski et al. 2013](#), hereafter M13), thus ensuring that no significant bias on the MDF can arise from kinematic cuts. The second criterion removes most of the foreground stars that happen to have proper motions within the adopted selection window, and it is justified by the fact that the parallax corresponding to the distance to the core of Sgr dSph (which we assume throughout the paper to be  $D = 26.3$ , from [Monaco et al. 2004](#)) is  $\omega \simeq 0.04 \text{ mas}$ , virtually indistinguishable from zero, within the typical uncertainty of the considered data ( $\text{err}_\omega \simeq 0.08 \text{ mas}$ ). From this sample, it is easy to select stars that sample the entire colour range spanned by the Sgr RGB, thus avoiding the biases against metal-poor stars that affected previous analyses. We also selected our targets only in the magnitude range  $16.0 < G < 17.4$  (approximately corresponding to  $16.4 < V < 17.8$ ), in order to avoid stars that are so cool that their spectra are strongly affected by TiO bands ([Monaco et al. 2005](#)) without introducing a colour cut that would bias the sample against the most metal-rich bright stars. We excluded stars whose light might be contaminated by close sources by selecting on the *Gaia* quality parameter `phot_bp_rp_excess_factor` ([Evans et al. 2018](#)) according to Eq. (C.2) of [Lindgren et al. \(2018\)](#)<sup>1</sup>. Finally, to avoid contamination of the light collected by individual FLAMES fibres from (relatively) bright sources near our spectroscopic targets, we excluded stars of magnitude  $G_\star$  with a companion closer than  $2.0''$  and brighter than

<sup>1</sup> That is, the following criterion on `E=phot_bp_rp_excess_factor`:  $1.0 + 0.015(G_{BP} - G_{RP})^2 < E < 1.3 + 0.06(G_{BP} - G_{RP})^2$ .

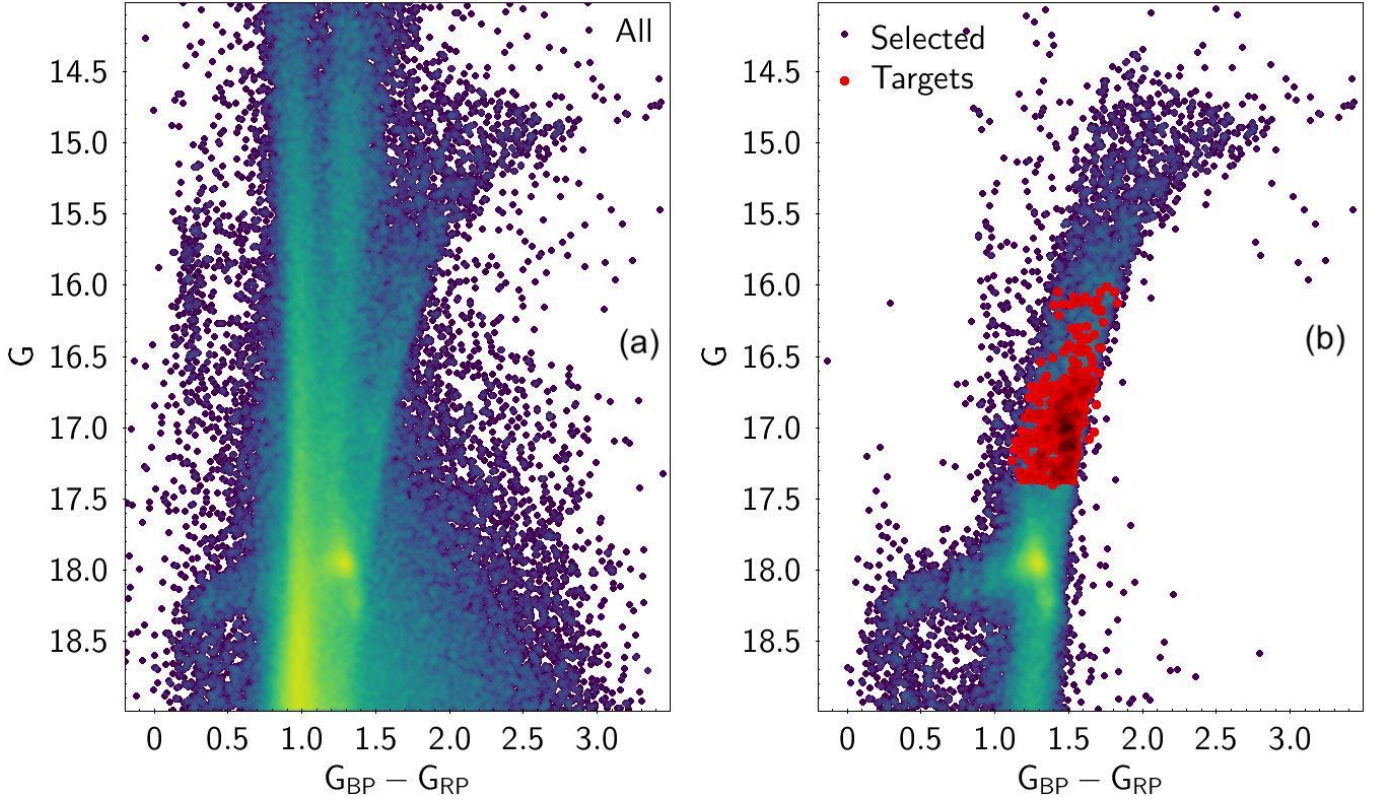


**Fig. 1.** *Gaia* DR3 CMD for Sgr: *Panel a:* *Gaia* DR3 CMD of a circle with a radius of  $1.0^\circ$  centred on the centre of Sgr dSph, from which the innermost nuclear region ( $R < 11.5'$ ) is excised. The stars are colour-coded according to the log of the local density. *Panel b:* Subset of the stars shown in panel a with a proper motion within  $0.5 \text{ mas year}^{-1}$  of the systemic motion of Sgr dSph and parallax within  $3\sigma$  from  $0.0 \text{ mas}$ . The 450 stars that are the object of this analysis are plotted in red.

$G = G_\star + 1.0$  (a common practice for this type of observations; see e.g., Carretta et al. 2009).

From the resulting sample, we extracted the stars in the four fields of view of the multi-object spectrograph GIRAFFE-FLAMES (mounted at the Very Large Telescope of ESO; Pasquini et al. 2002) that are located around the nuclear region of Sgr, as shown in Fig. 2. Then, the 450 stars observed in the four fields were selected by the automated fibre-allocation procedure. Once again, this should prevent any bias on metallicity or RV on the stars of our final sample, shown as red dots in Fig. 1 and as dots coloured according to the specific FLAMES field in Fig. 2.

All the spectra were acquired with the GIRAFFE-FLAMES HR21 setup (spectral range  $8484\text{--}9001 \text{ \AA}$  and resolving power  $\frac{\lambda}{\Delta\lambda} \simeq 18000$ ). The observations were collected under the ESO program 105.20AH.001 (PI: Bellazzini). Observations should have been carried out in 2020, but they were postponed to 2021 because of the restrictions to ESO observatory operations due to the Covid19 pandemic, and they took place between 28th June and 5th July 2021. At the epoch, the sample selection was performed on the *Gaia* DR2 catalogue (Gaia Collaboration 2018a). We verified that the selected stars remain bona fide candidate members of the main body of Sgr if astrometry from *Gaia* EDR3 (Gaia Collaboration 2021) is used instead. We only used EDR3 astrometry and photometry (Riello et al. 2021).

For each field, two  $t_{\text{exp}} = 2775 \text{ s}$  exposures were acquired. The spectra were reduced with the dedicated ESO pipeline<sup>2</sup> that performs the bias subtraction, flat-fielding, wavelength cali-

bration, spectral extraction, and order merging. The individual exposures were sky-subtracted using the average spectrum of some close sky regions observed at the same time of the science targets, and then they were combined into a single spectrum for each star, in order to reach a signal-to-noise ratio per pixel of at least 40 for the faintest and 75 for the brightest stars.

### 3. Atmospheric parameters

For all the selected targets, we have accurate *Gaia* EDR3 photometry ( $G$  and  $G_{BP} - G_{RP}$ ), from which we can obtain the atmospheric parameters in a homogeneous way. Effective temperatures ( $T_{\text{eff}}$ ) were derived using the  $(BP - RP)_0 - T_{\text{eff}}$  transformation by Mucciarelli et al. (2021) and adopting  $E(B - V)$  from the reddening maps of Schlegel et al. (1998), as recalibrated by Schlafly & Finkbeiner (2011). The mean values of  $E(B - V)$  are  $0.122 \pm 0.003$ ,  $0.126 \pm 0.004$ ,  $0.133 \pm 0.005$ , and  $0.138 \pm 0.002$  for fields 1–4, respectively (see Fig. 2). Surface gravities were derived following the iterative procedure described by Lombardo et al. (2021, their Sect. 4.1), adopting  $T_{\text{eff}}$  derived above and the distance of  $D = 26.3 \text{ kpc}$  from Monaco et al. (2004), and calculating the G-band bolometric correction  $BC(G)$  by interpolating (at fixed metallicity and  $T_{\text{eff}}$ ) in a grid of theoretical  $BC(G)$  values obtained from ATLAS9 model atmospheres.

The microturbulent velocities  $v_t$  were derived from the relation of Mucciarelli & Bonifacio (2020) according to the log  $g$  and the metallicities of the stars. Since the atmospheric parameters derived in this way depend on the adopted metallicity value,

<sup>2</sup> <http://www.eso.org/sci/software/pipelines/>

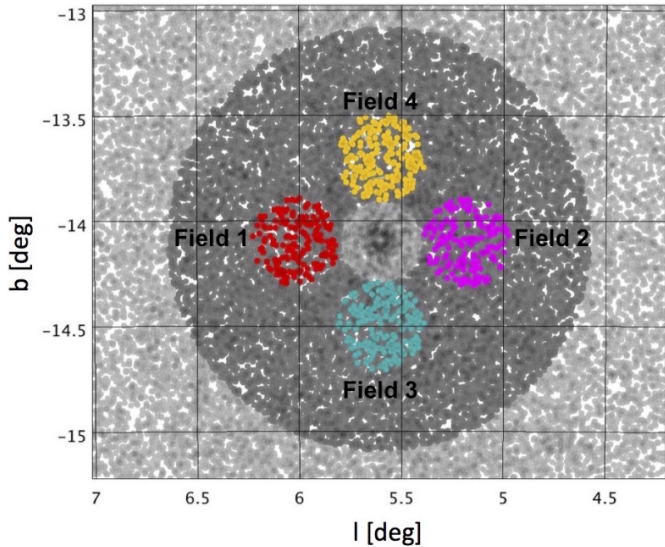


**Fig. 2.** Map of the central region of Sgr dSph. Only stars selected as likely members of the dwarf are plotted. Stars in the range  $11.5' < R < 60.0'$  are plotted as filled dark grey circles. The observed spectroscopic targets in the four FLAMES fields are shown as filled coloured circles.

the procedure was repeated, updating all the parameters at each step, until convergence.

Uncertainties in  $T_{\text{eff}}$  are dominated by the uncertainty in the adopted colour- $T_{\text{eff}}$  transformation ( $\sim 80$  K; see Mucciarelli et al. 2021), while the contribution by photometry and reddening errors is negligible (less than 10 K). Uncertainties in  $\log g$  are about 0.1, including the contribution of errors in  $T_{\text{eff}}$ , adopted distance, and stellar mass. Finally, we assumed a typical error of  $0.2 \text{ km s}^{-1}$  for  $v_t$  according to the uncertainties in  $\log g$  and in the adopted  $v_t$ - $\log g$  calibration.

The final atmospheric parameters for the stars in our sample are listed in Table 1, together with their coordinates, *Gaia* EDR3 photometry, and the measured RVs and metallicities.

## 4. Analysis

### 4.1. Radial velocity

Heliocentric RV measures were obtained with DAOSPEC (Stetson & Pancino 2008), which automatically finds the centroid of spectral lines by Gaussian fitting. The final RV is the mean derived from the wavelength shift of the  $N$  measured lines, and the associated uncertainty is the standard deviation divided by  $\sqrt{N}$ .

The final spectra of 31 of the 450 observed stars were affected by particularly strong residuals of sky subtraction. For these stars, we preferred to derive the RV interactively by measuring the wavelength shift for the CaII triplet lines using the IRAF task *splot*. We conservatively assigned an uncertainty of  $1.0 \text{ km s}^{-1}$  to these stars, which is a strong upper limit to the distribution of the measured RV uncertainties. The uncertainties in RV range from  $0.2 \text{ km s}^{-1}$  to  $1.0 \text{ km s}^{-1}$ , and 80% of the sample have  $\text{err}_{\text{RV}} < 0.5 \text{ km s}^{-1}$ .

### 4.2. Metallicity

The chemical abundances were then derived using our own code SALVADOR, which performs a  $\chi^2$  minimisation between the observed line and a grid of suitable synthetic spectra calcu-

lated on the fly using the code SYNTHE (Kurucz 2005) and varying only the abundance of the corresponding element. Model atmospheres were calculated for each star with the code ATLAS9 (Kurucz 1993, 2005). The lines were selected in order to avoid blended or saturated lines, and we kept only transitions that were not affected by residuals of the sky subtraction. The number of Fe lines we used changed with the metallicity, atmospheric parameters, and noise of the spectra. We used from 2 (1% of the sample) to 19 lines (0.5% of the sample). The median value of the number of Fe lines is 15.

To determine the uncertainty, two main sources of error were taken into account: the error arising from the measurement procedure, and that arising from the uncertainty in atmospheric parameters. The first was computed as the standard deviation of the Fe abundance measures, divided by the square root of the number of lines used to derive the metallicity. The error in  $[\text{Fe}/\text{H}]$  arising from the uncertainties in the adopted parameters was estimated by repeating the analysis of all the stars by varying the parameters of the corresponding errors, as estimated in Sect. 3. This uncertainty was added in quadrature to the statistical error associated with the mean  $[\text{Fe}/\text{H}]$  of each star. The uncertainties in  $[\text{Fe}/\text{H}]$  range from 0.02 dex to 0.24 dex, and 80% of the sample have  $\text{err}_{[\text{Fe}/\text{H}]} \leq 0.1$  dex.

## 5. Results

### 5.1. Radial velocity distribution

The RV distribution of the analysed stars is shown in Fig. 3 as a function of the angular distance from the centre of the Sgr dSph galaxy. Following Ibata et al. (1997), we considered bona fide Sgr members the stars with RV between  $+100 \text{ km s}^{-1}$  and  $+180 \text{ km s}^{-1}$ . All the observed stars fulfil this requirement. Therefore, the success rate of the adopted selection of candidate Sgr member stars is 100%, to be compared with typical rates  $< 80\%$  for best-effort pre-*Gaia* purely photometric selections. For example only  $\approx 73\%$  of the candidate Sgr RGB stars surveyed by Bellazzini et al. (2008) were confirmed as bona fide members of the dwarf galaxy based on their RV (843 of 1152 stars).

This result confirms that proper selections based on *Gaia* astrometry, in addition to preventing any metallicity bias, can be extremely efficient in selecting galaxy members, and should be adopted to maximise the scientific return of future spectroscopic surveys devoted to study Sgr stars, such as those planned with MOONS<sup>3</sup> at the VLT (Cirasuolo et al. 2020; Gonzalez et al. 2020).

The radial range spanned by our data is  $11.5' \lesssim R \lesssim 36.2'$ , corresponding to  $88 \text{ pc} \lesssim R \lesssim 277 \text{ pc}$ , to be compared to the core radius of the dwarf galaxy,  $r_c = 224' \pm 12'$ , corresponding to  $r_c = 1720 \pm 100 \text{ pc}$ , as determined by Majewski et al. (2003). Hence, while avoiding the nuclear region, we sample the very central part of the Sgr core.

The RV distribution of Fig. 3 is fully compatible with previous results in the literature (Ibata et al. 1997; Bellazzini et al. 2008; M13). The velocity dispersion profile is flat within the uncertainties. The mean velocity and intrinsic velocity dispersion for the entire sample, estimated with the simple maximum likelihood procedure described in Pryor & Meylan (1993) and Walker et al. (2006), are  $\langle \text{RV} \rangle = 142.9 \pm 0.5 \text{ km s}^{-1}$  and  $\sigma_{\text{int}} = 11.6 \pm 0.4 \text{ km s}^{-1}$  (see also Table 2 for fully compatible estimates obtained with a slightly different technique).

<sup>3</sup> Multi Object Optical and Near-infrared Spectrograph.

**Table 1.** Main parameters of the target stars.

| <i>Gaia</i> DR3 ID  | RA<br>[deg] | Dec<br>[deg] | <i>G</i><br>[mag] | <i>BP</i><br>[mag] | <i>RP</i><br>[mag] | $T_{\text{eff}}$<br>[K] | $\log g$<br>[ $\text{cm s}^{-2}$ ] | $v_t$<br>[ $\text{km s}^{-1}$ ] | RV<br>[ $\text{km s}^{-1}$ ] | err<br>[ $\text{km s}^{-1}$ ] | [Fe/H]<br>[dex] | err<br>[dex] |
|---------------------|-------------|--------------|-------------------|--------------------|--------------------|-------------------------|------------------------------------|---------------------------------|------------------------------|-------------------------------|-----------------|--------------|
| 6760458745060096384 | 284.031     | -30.242      | 16.78             | 17.50              | 15.96              | 4444                    | 1.66                               | 1.5                             | 137.4                        | 0.3                           | -0.41           | 0.08         |
| 6760462318472909312 | 284.057     | -30.175      | 16.79             | 17.55              | 15.94              | 4341                    | 1.60                               | 1.5                             | 143.1                        | 0.3                           | -0.43           | 0.09         |
| 6761208779461501184 | 283.796     | -30.150      | 16.82             | 17.58              | 15.98              | 4346                    | 1.62                               | 1.5                             | 140.7                        | 0.3                           | -0.44           | 0.10         |
| 6760455446525277056 | 283.894     | -30.276      | 16.82             | 17.50              | 16.02              | 4524                    | 1.71                               | 1.5                             | 150.2                        | 0.4                           | -0.75           | 0.07         |
| 6760462898263096832 | 283.947     | -30.174      | 16.84             | 17.50              | 16.07              | 4605                    | 1.78                               | 1.4                             | 146.6                        | 0.3                           | -0.46           | 0.06         |
| ...                 |             |              |                   |                    |                    |                         |                                    |                                 |                              |                               |                 |              |

**Notes.** The full version of the table is available at the CDS.

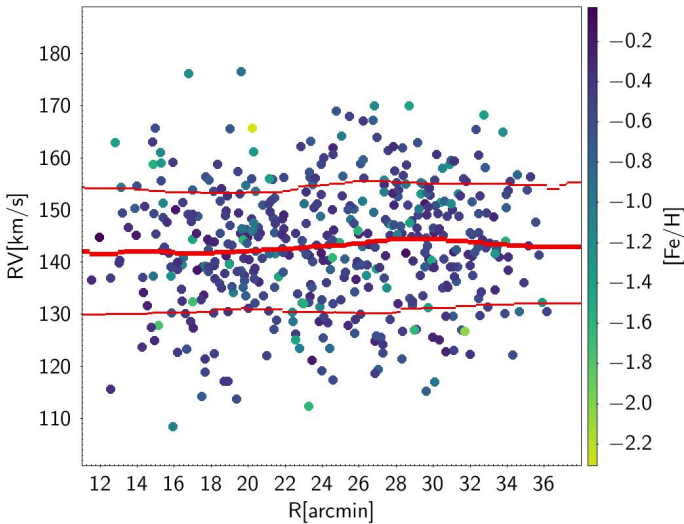


**Fig. 3.** Radial velocity of the surveyed stars as a function of the angular distance from the centre of the Sgr galaxy. Stars are colour-coded according to their iron abundance. The thick red line is the running median smoothed over  $8'$  radial bins, while the thin red lines mark the 16th and 84th percentiles of the RV distribution, with the same smoothing, approximately enclosing the  $\pm 1\sigma$  interval about the systemic velocity.

## 5.2. Metallicity distribution

The first unbiased MDF of the core of Sgr dSph is shown in Fig. 4. In overall agreement with previous results in the literature (see e.g., Bellazzini et al. 2008; Hasselquist et al. 2017, 2021; Hayes et al. 2020; M17, and references therein), the distribution is dominated by a strong, relatively narrow, and symmetric peak at  $[\text{Fe}/\text{H}] \simeq -0.5$ , and it displays a weak but extended tail reaching  $[\text{Fe}/\text{H}] \lesssim -2.0$ .

We used the Mclust package (Scrucca et al. 2016) within the R environment<sup>4</sup> to parametrise the distribution with a simple Gaussian mixture model. Mclust uses the Bayesian information criterion (BIC) to select the number of mixing components. The preferred model consists of two Gaussian components with  $(\mu_1, \sigma_1) = (-0.47, 0.13)$  and  $(\mu_2, \sigma_2) = (-1.05, 0.39)$ , respectively; the main metal-rich component accounts for 74.4% of the sample and the broad metal-poor component accounts for the remaining 25.6%. Unfortunately, Mclust does not take into account uncertainties in individual measures, hence we used to a maximum likelihood procedure to estimate the intrinsic values of the model parameters and the associated uncertainties. Since the  $[\text{Fe}/\text{H}]$  errors are small, the values are very similar to

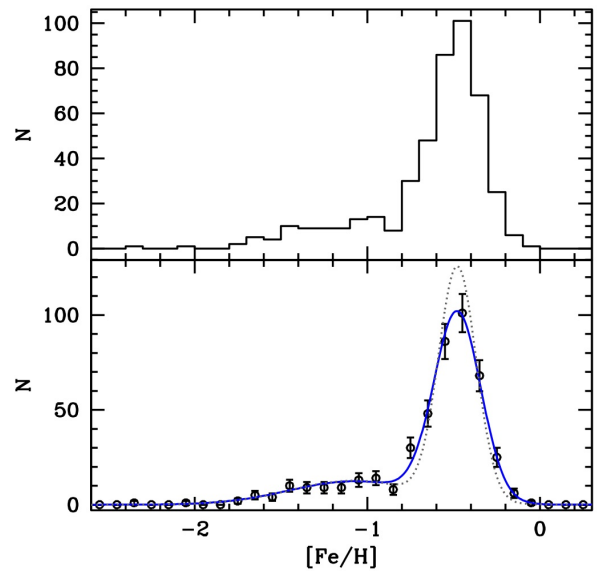


**Fig. 4.** Upper panel: metallicity distribution of the target stars displayed as a normal histogram. Lower panel: same distribution represented as points with Poisson error bars. The dotted grey curve is the best-fit two-Gaussian model with the estimated intrinsic  $\sigma$  values, while the continuous blue curve is the same model convolved with the mean uncertainty of individual  $[\text{Fe}/\text{H}]$  measures (0.08 dex).

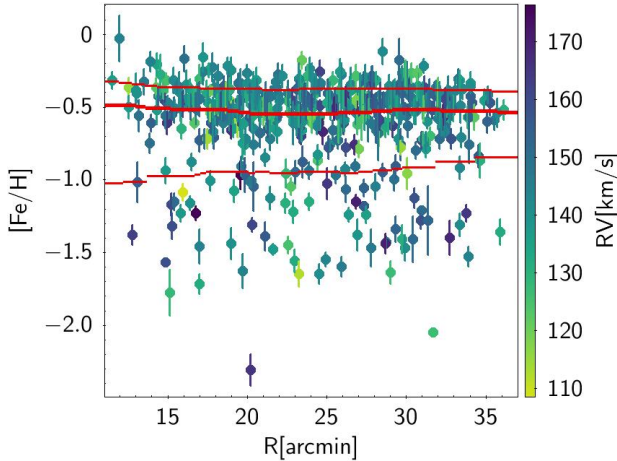
those derived with Mclust, that is,  $(\mu_1, \sigma_1^{\text{int}}) = (-0.478 \pm 0.008, 0.109 \pm 0.007)$  and  $(\mu_2, \sigma_2) = (-1.077 \pm 0.057, 0.368 \pm 0.032)$ , with the fraction of stars in the first component  $f_1 = 0.755 \pm 0.030$ .

Figure 5 shows that in the limited radial range covered by our data, no significant signs of a metallicity gradient are detected. The asymmetry and the two-component nature of the overall MDF is strikingly evident here.

In the upper panel of Fig. 6, we compare our MDF with those derived by Hayes et al. (2020, H20 hereafter) from APOGEE<sup>5</sup> (Majewski et al. 2017) spectra of a large sample of Sgr stars belonging both to the main body and the stream, selected according to their angular momentum. The agreement with the H20 main body sample is quite good. The same is true for the larger sample of APOGEE DR17 (Abdurro'uf et al. 2022) Sgr members that we selected following Hasselquist et al. (2021, H21 sample hereafter), shown in the lower panel of Fig. 6. In addition to the general criteria described in Sect. 3 of Hasselquist et al. (2021), we selected Sgr members according to their RV ( $100 < \text{RV} < 180 \text{ km s}^{-1}$ ), their distance from the Sgr centre (within  $5.0'$ , and outside  $15.0'$ , to avoid the nuclear region), their *Gaia* proper motions (same selection adopted for

<sup>4</sup> <https://www.r-project.org>

<sup>5</sup> Apache Point Observatory Galactic Evolution Experiment.



**Fig. 5.** Iron abundance of the surveyed stars as a function of the angular distance from the centre of the Sgr galaxy. Stars are colour-coded according to their RV. The thick red line is the running median smoothed over 8' radial bins, while the thin red lines mark the 16th and 84th percentiles of the [Fe/H] distribution.

our sample), and, finally, their position on the CMD, excluding stars that were obvious outliers of the RGB.

In the main body, the overall agreement between our MDF and those shown in Fig. 6 suggests that the metallicity biases affecting the considered APOGEE samples are quite mild, and, in general, there are no large undetected populations of metal-poor stars hidden in the Sgr core (as suggested also by the abundance of blue horizontal branch stars; see Monaco et al. 2003, and references therein). Still, a small bias against metal-poor stars is there and can be measured. The H20 main body sample and the H21 sample contain 710 and 1034 bona fide Sgr member stars, respectively, but no star with  $[\text{Fe}/\text{H}] < -2.0$ , while we have two such stars over 450 ( $0.4 \pm 0.3\%$ ). The fraction of stars with  $[\text{Fe}/\text{H}] < -1.5$  ( $[\text{Fe}/\text{H}] < -1.0$ ) is  $1.5 \pm 0.5\%$  ( $11.5 \pm 1.3\%$ ) and  $0.5 \pm 0.2\%$  ( $10.8 \pm 2.7\%$ ) in the H20 main body and H21 samples, respectively, to be compared with  $2.9 \pm 0.8\%$  ( $13.8 \pm 1.9\%$ ) in our sample. The metal-poor population is slightly under-represented in the H20 and H21 samples with respect to ours, in spite of the much larger radial range spanned by their stars (as the large-scale radial gradient should make metal-poor stars more frequent at large distances from the galaxy centre; Vitali et al. 2022, while we sample the most central part of the main body core).

On the other hand, the comparison with the H20 MDF of the stream confirms the strong difference between the chemical composition of stars in the main body and the stream, suggesting that a large fraction of the most metal-poor component of the Sgr progenitor was stripped from the main body during the tidal disruption process (Chou et al. 2007; Monaco et al. 2007; Law & Majewski 2010; Gibbons et al. 2017; Hayes et al. 2020; Johnson et al. 2020, and references therein). In particular, the selection-corrected MDF of the Sgr stream by Johnson et al. (2020) has a mean  $[\text{Fe}/\text{H}] = -0.99$ , very few stars with  $[\text{Fe}/\text{H}] > -0.5$ , and 3% of stars with  $[\text{Fe}/\text{H}] < -2.0$ . Hence, very metal-poor stars are a factor of  $\approx 7$  more abundant in their stream sample than in our main body sample.

### 5.3. Comparison with other MW satellites

In Fig. 7 we compare our Sgr MDF with those of three dwarf satellites of the MW spanning a range of stellar masses (taken

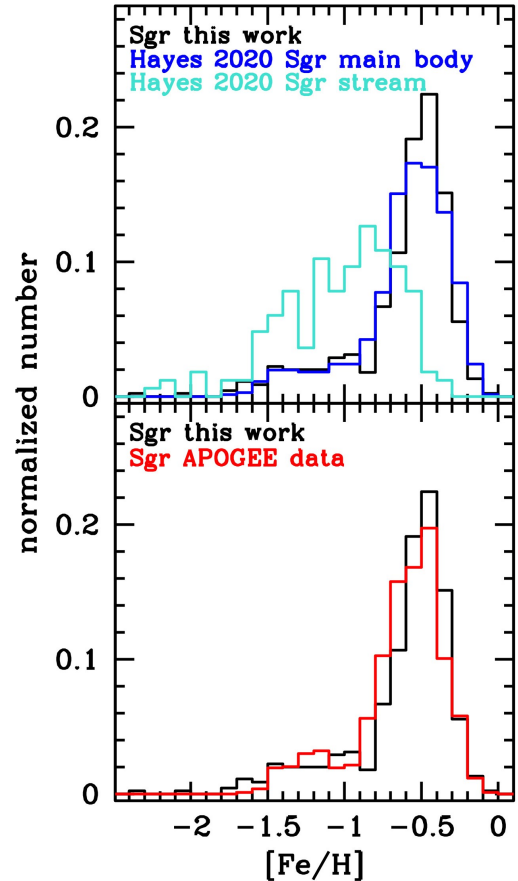


**Fig. 6.** Upper panel: comparison between the metallicity distribution derived in this work (black line) with those derived by Hayes et al. (2020, H20 samples) for Sgr main body (blue line; 710 stars) and Sgr stream stars (light blue line; 166 stars). Lower panel: Same comparison, but with the Sgr APOGEE DR17 H21 sample (red line; 1034 stars). The distributions are normalised to have a unit area.

from McConnachie 2012) that brackets the value for the Sgr main body by Vasiliev & Belokurov (2020): from about 10 times lower ( $2.0 \times 10^7 M_{\odot}$ , Fornax dSph)<sup>6</sup> to similar ( $4.6 \times 10^8 M_{\odot}$ , Small Magellanic Cloud, SMC hereafter) and to  $\geq 10$  larger than it ( $1.5 \times 10^9 M_{\odot}$ , Large Magellanic Cloud, LMC hereafter). The latter value is probably overestimated (see Vasiliev & Belokurov 2020), but we are mainly interested in providing an idea of the involved mass ranking and range. In these cases, the samples were selected from APOGEE DR17, exactly as was done in Hasselquist et al. (2021).

The MDFs of the four galaxies are fairly similar in shape: They all have a strong and relatively narrow peak on the metal-rich side, within  $\lesssim 0.5$  dex of their most iron rich stars, and a weak tail extending in the metal-poor regime. The main difference lies in the position of the peak. In this sense, the comparison is not fair, as the various samples cover hugely different radial ranges within the different galaxies, and we know that the disruption process has preferentially removed metal-poor stars from the progenitor of Sgr. Still, it is remarkable that the peak of the MDF of the main body of Sgr is significantly more metal-rich than that of the other galaxies considered here, and the fraction of stars with  $[\text{Fe}/\text{H}] \geq -0.5$  for example is much larger than that observed in the MDF of the LMC. This provides some sup-

<sup>6</sup> Note, however, that McConnachie (2012) reported  $M_{\star} = 2.1 \times 10^7 M_{\odot}$  for Sgr dSph.

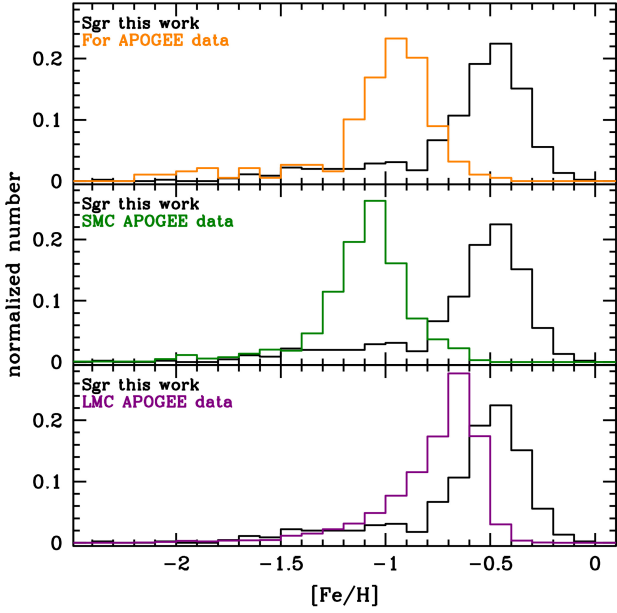


**Fig. 7.** Comparison between the metallicity distribution derived in this work (black line) with those from APOGEE DR17 data for different galaxies: Fornax (orange line; 189 stars) in the upper panel, SMC (green line; 1031 stars) in the middle panel, and LMC (violet line; 3897 stars) in the lower panel. The distributions are normalised to have a unit area.

port to the idea of a fairly massive progenitor of Sgr, possibly comparable to the LMC (Monaco et al. 2005; Łokas et al. 2010; Niederste-Ostholt et al. 2012; de Boer et al. 2014; Gibbons et al. 2017; Carlin et al. 2018; Minelli et al. 2021; Johnson et al. 2020; M17).

#### 5.4. Comparison with chemical evolution models

The MDF is an important constraint in chemical evolution studies. In particular, it allows breaking severe degeneracies in chemical evolution model parameters that would remain in place if only the run of abundance ratios with metallicity were considered (see e.g., Romano et al. 2015, their Figs. 1 and 2). It is well known that the effects of changes in several free parameters of the models tend to cancel out when the ratios of the abundances of different chemical species are considered (Tosi 1988).

Figure 8 shows the comparison between the MDF of the core of Sgr derived in this work and those predicted by two chemical evolution models that prove able to fit the main chemical properties of Sgr. The models are the one presented and discussed in M17, and a new version of the same model that was slightly modified to explore the case of a more massive progenitor. In the following, we recall their main properties (see Romano et al. 2015, for more details and definitions).

First we note that our models aim at reproducing the chemical properties of the progenitor of the Sgr system. The bulk of the stellar populations of Sgr is assumed to have formed from 14 to 7 Gyr ago (see M17 for discussion and references). The Sgr progenitor is then assumed to start losing a large fraction of its gas due to the interaction with the MW, until the star formation definitively stops, about 6 Gyr ago. Figure 13 of M17 shows that the run of several abundance ratios with  $[\text{Fe}/\text{H}]$  can be reasonably well explained within this evolutionary framework.

M17 assumed that  $2 \times 10^9 M_{\odot}$  of gas are accreted on short timescales,  $\tau = 0.5$  Gyr, and are converted into stars with an efficiency  $\nu = 0.1 \text{ Gyr}^{-1}$ , until the progenitor reaches a mass in stars

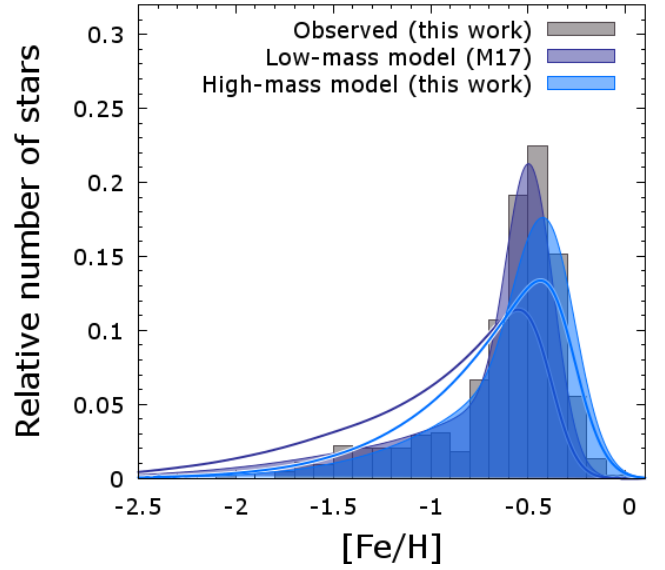


**Fig. 8.** Comparison between the MDF derived in this work (grey shaded histogram) and those predicted from the chemical evolution models by M17 and its revised version presented here. The MDF from the original models is presented as the empty curves, while the coloured shaded curves show the same distributions after removal of 75% (M17 model) and 50% (new model) of the metal-poor stars ( $[\text{Fe}/\text{H}] < -0.6$ ). The distributions are normalised to have a unit area.

of  $\sim 7 \times 10^8 M_{\odot}$ . At this point, the satellite starts to be stripped by the Milky Way. Here, we assumed a higher initial gaseous mass for the progenitor,  $4.2 \times 10^9 M_{\odot}$ , a longer timescale for gas accretion,  $\tau = 3$  Gyr, and a higher efficiency of conversion of gas into stars,  $\nu = 0.2 \text{ Gyr}^{-1}$ . The mass in stars at the beginning of the interaction with the Milky Way is  $1.6 \times 10^9 M_{\odot}$ , that is, we considered a LMC-like Sgr precursor. While we are still able to fit the same  $[\text{X}/\text{Fe}]$ – $[\text{Fe}/\text{H}]$  trends as M17, we now also produce a theoretical MDF peaking at the right  $[\text{Fe}/\text{H}]$  value spotted out by the current observations, and with much less power in the metal-poor tail than the M17 model.

In any case, both models over-predict the fraction of metal-poor stars with respect to the observed MDF, providing additional support to the hypothesis that the process of tidal stripping removed preferentially metal-poor stars from the Sgr progenitor (see e.g., Law & Majewski 2016, and references therein). To provide a qualitative idea of the effects of this process, in Fig. 8 we also show the MDF of the two models after removal of 50% and 75% of the stars with  $[\text{Fe}/\text{H}] < -0.6$  from the new model and the M17 model, respectively. The metal-poor side of the observed MDF can now be broadly matched, and the main peak becomes stronger and narrower, more similar to its observed counterpart.

This comparison should be considered only as an insightful exercise, showing that the observed MDF is consistent with a simple but physically motivated chemical evolution model plus preferential stripping of metal-poor stars. The results would not change much if, for example, the MDF from the H21 sample were considered instead of the one derived here, as the differences are small (Sect. 5.2). It must be realised that a fully quantitative comparison with chemical evolution models is clearly impossible for a disrupting galaxy with a metallicity gradient. This formidable task could be attempted only with a self-consistent chemodynamical model following the evolution of all the components of the progenitor (gas, stars, and dark matter), its star formation history, chemical evolution history, the interaction



of its gas component with the Milky Way disc and corona, and the process of its tidal disruption.

### 5.5. Correlation between kinematics and metallicity

In addition to a metallicity gradient within the main body and along the stream, [Gibbons et al. \(2017\)](#) recently found that the typical MDF in the stream is made up of two components, and that the metal-poor (MP) component is kinematically hotter than its metal-rich (MR) counterpart. On the other hand, [Johnson et al. \(2020\)](#) found that the kinematics of the most metal-poor component ( $[\text{Fe}/\text{H}] < -1.9$ ) in their Sgr stream sample significantly differs from that of the bulk of more metal-rich component both in terms of velocity dispersion and of mean velocity in the Galactic reference frame. Chemical abundance differences between the different branches and sub-branches of the Sgr stream are discussed in detail in [Ramos et al. \(2022\)](#).

The generally accepted interpretation of these features is that there was a metallicity gradient in the progenitor of Sgr, as observed in most dwarf galaxies ([Harbeck et al. 2001](#); [Taibi et al. 2022](#)), with the MP component being more extended and with a higher velocity dispersion than the MR one, as observed for example in the Sculptor dSph ([Tolstoy et al. 2004](#)), Fornax dSph ([Battaglia et al. 2006](#)), and other local dwarf galaxies (see [Battaglia & Nipoti 2022](#), for a recent review). For its structural and kinematic properties, the metal-poor component was presumably preferentially stripped from the progenitor in the early phases of its disruption in a progressive peeling off of its composite stellar population. In particular, [Johnson et al. \(2020\)](#) suggested that the diffuse MP population originates from an extended metal-poor halo that surrounded the progenitor of Sgr.

On the opposite side of the huge range of scales spanned by the Sgr system, [Alfaro-Cuello et al. \(2020\)](#) found significant differences in the kinematics of the three components identified in the innermost region of the stellar nucleus ( $R \leq 3.5' \approx 25$  pc). However, the velocity dispersion curves and rotation curves obtained by [Alfaro-Cuello et al. \(2020\)](#) are limited to  $R \leq 2.0' \approx 15$  pc, essentially for reasons of binning. (see also [Bellazzini et al. 2008](#); [Carlberg & Grillmair 2022](#)). However, two of these components, the young metal-rich (YMR) and the old metal-poor (OMP) ones, according to their nomenclature, are characteristic of the nuclear cluster and confined within the narrow region that we purposely avoided to obtain an unbiased MDF representative of the main body. In particular, the OMP in the nuclear region is dominated by the globular cluster M 54 ([Carlberg & Grillmair 2022](#)). The only component that can be related to the stellar population studied here is their intermediate-age metal-rich (IMR) population, which can be considered as the innermost counterpart of our MR population, but the actual selection windows are not strictly equivalent.

While these chemo-kinematic differences have been analysed in some detail in the Sgr stream ([Gibbons et al. 2017](#); [Johnson et al. 2020](#)) and in the stellar nucleus ([Alfaro-Cuello et al. 2020](#)), the situation in the main body is much less explored. The only indication of a possible difference in velocity dispersion between the MR and MP components in the main body was provided by M13. Using a sample of 328 members within  $\approx 1^\circ$  from the centre of the dwarf galaxy, they highlighted a systematic difference in the velocity dispersion curves of the stars above and below  $[\text{Fe}/\text{H}] = -0.4$ , the most MP sub-sample displaying slightly higher values of the velocity dispersion than the MR one over the entire radial range covered.

**Table 2.** Median values of the parameters of the kinematic models.

| Par                                                           | MR sample          | MP sample          | All                |
|---------------------------------------------------------------|--------------------|--------------------|--------------------|
| $N_*$                                                         | 294                | 156                | 450                |
| $\langle \text{RV} \rangle$ [ $\text{km s}^{-1}$ ]            | $141.8 \pm 0.6$    | $144.4 \pm 1.0$    | $142.8 \pm 0.5$    |
| $\sigma_{\text{int}}$ [ $\text{km s}^{-1}$ ]                  | $10.5 \pm 0.4$     | $13.3 \pm 0.8$     | $11.6 \pm 0.4$     |
| $V_{\text{rot}}$ [ $\text{km s}^{-1}$ ]                       | $3.1 \pm 0.9$      | $1.8 \pm 1.2$      | $2.0 \pm 0.8$      |
| PA[deg]                                                       | $116.3 \pm 17.5$   | $57.2 \pm 42.5$    | $94.7 \pm 24.2$    |
| $\langle \text{pmra} \rangle$ [ $\text{mas yr}^{-1}$ ]        | $-2.673 \pm 0.007$ | $-2.694 \pm 0.011$ | $-2.680 \pm 0.006$ |
| $\langle \text{pmdec} \rangle$ [ $\text{mas yr}^{-1}$ ]       | $-1.387 \pm 0.006$ | $-1.400 \pm 0.009$ | $-1.392 \pm 0.005$ |
| $\sigma_{\text{int}}^{\text{pmra}}$ [ $\text{mas yr}^{-1}$ ]  | $0.103 \pm 0.006$  | $0.137 \pm 0.009$  | $0.117 \pm 0.005$  |
| $\sigma_{\text{int}}^{\text{pmdec}}$ [ $\text{mas yr}^{-1}$ ] | $0.087 \pm 0.005$  | $0.118 \pm 0.007$  | $0.100 \pm 0.004$  |
| $\rho$                                                        | $0.255 \pm 0.080$  | $0.123 \pm 0.088$  | $0.195 \pm 0.060$  |

**Notes.** The median  $\pm \sigma$  of the posterior PDF are reported, where  $\sigma$  is estimated as half the interval between the 16th and 84th percentile of the distribution. All the marginalised PDFs are bell-shaped and remarkably symmetric.

We used our new dataset to follow this result up. With respect to M13, our sample is slightly larger and confined to a more restricted radial range. However, as expected, it provides a significantly extended sampling of the metal-poor population because only six of the stars analysed by M13 reach  $[\text{Fe}/\text{H}] < -1.0$  (see their Fig. 2h).

As a first step, we compared the RV distributions of the sub-samples with a metallicity above or below a certain threshold  $[\text{Fe}/\text{H}]_{\text{tresh}}$  using the Kolmogorov–Smirnov (KS) statistical test. The probability that the two sub-samples are extracted from the same parent RV distribution is lower than 5.0% for thresholds in the range  $-0.6 \leq [\text{Fe}/\text{H}]_{\text{tresh}} \leq -1.0$ , with a minimum of  $P_{\text{KS}} < 0.5\%$  at  $[\text{Fe}/\text{H}]_{\text{tresh}} = -0.6$ . We adopted this value to divide our sample into an MR sub-sample ( $[\text{Fe}/\text{H}] \geq -0.6$ ; 294 stars) and an MP sub-sample ( $[\text{Fe}/\text{H}] < -0.6$ ; 156 stars).

To gain deeper insight into the nature of the kinematic differences between the two sub-samples, we analysed them separately, as well as the entire sample, using a Bayesian approach. Monte Carlo Markov chains (MCMC) were used to explore the posterior probability density function (PDF) of the four parameters of the simple Gaussian model with rotation described by [Kamann et al. \(2018\)](#): mean  $\langle \text{RV} \rangle$ , intrinsic velocity dispersion  $\sigma_{\text{int}}$ , amplitude of rotation  $V_{\text{rot}}$  along the line of sight, and the position angle of the projected rotation axis PA, measured from north toward east. We adopted a broad Gaussian prior for  $\langle \text{RV} \rangle$ , with mean  $\mu = 143.0 \text{ km s}^{-1}$  and  $\sigma = 100.0 \text{ km s}^{-1}$ , uniform priors in the range  $0.0\text{--}30.0 \text{ km s}^{-1}$  for both  $\sigma_{\text{int}}$  and  $V_{\text{rot}}$ , and a uniform prior in the range  $0.0^\circ\text{--}180.0^\circ$  for PA. To sample the posterior PDF, we used JAGS<sup>7</sup>, within the R environment, to run five independent MCMCs of 20 000 steps each after a burn-in phase of 1000 steps for each chain. Results on rotation, and in particular, the constraints on the position angle, must be considered with caution because of the non-uniform distribution in azimuth of our sample (see Fig. 2), which may lead to an odd sampling of the underlying velocity field. Our purpose is to search for differences between the kinematics of the two sub-samples in terms of ordered motions as well.

The main results are summarised Table 2 and illustrated in Fig. 9. While the possibility that the two sub-samples are adequately described with models having the same parameters cannot be completely ruled out, their PDFs are remarkably different. In particular, the velocity distribution of MP stars indicates a higher velocity dispersion than the MR sample. On the other hand,

<sup>7</sup> <http://mcmc-jags.sourceforge.net>

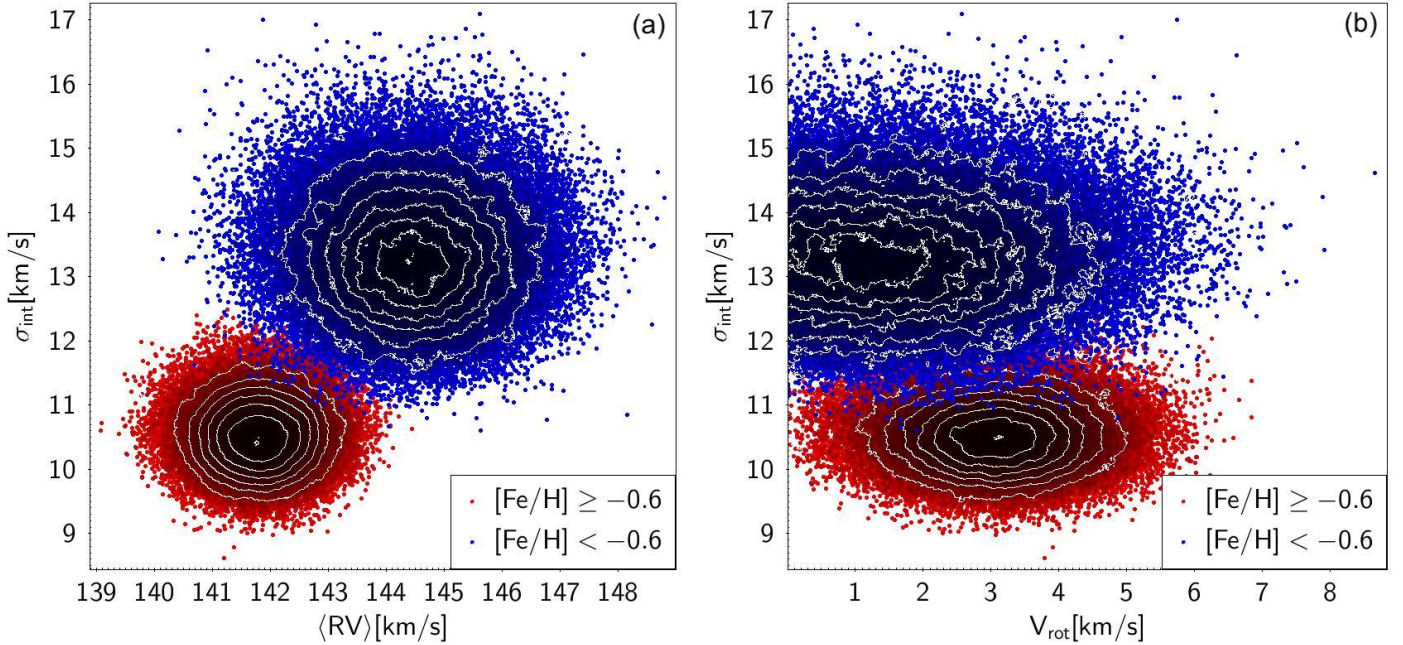


**Fig. 9.** 2D posterior PDF of key parameters of the adopted kinematic model for the MP (blue points) and the MR (red points) sub-samples, as sampled with the MCMC. *Panel a:*  $\langle RV \rangle$  and  $\sigma_{\text{int}}$ . *Panel b:*  $V_{\text{rot}}$  and  $\sigma_{\text{int}}$ .

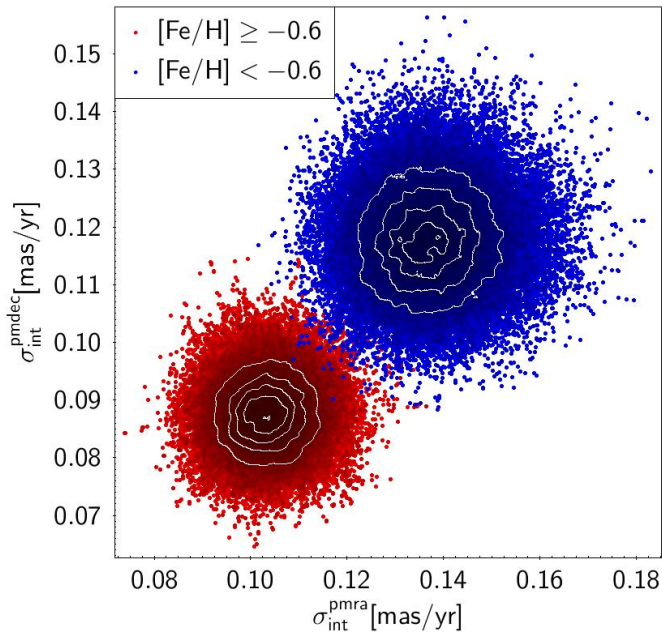


**Fig. 10.** 2D posterior PDF of the proper motion dispersions for the MP (blue points) and the MR (red points) sub-samples, as sampled with the MCMC.

the observed MR velocities are hardly compatible with null values of  $V_{\text{rot}}$ , while the rotation signal is null or weak in the MP sample. We compared sub-samples spanning the same small radial range, hence perspective rotation (Vasiliev & Belokurov 2020) cannot play any role in the detected difference in the PDFs of  $V_{\text{rot}}$  between the MR and MP sub-samples. This confirms the earlier findings by M13 about the correlation between velocity dispersion and chemical composition in the Sgr core. Because of the different radial range and the stellar nucleus, the comparison with the results of Alfaro-Cuello et al. (2020) is much more difficult. Considering their IMR component as an approximate counterpart

of the MR sub-sample considered here, we note that they found that it displays a weak rotation ( $\sim 2 \text{ km s}^{-1}$ ), in broad agreement with our results. On the other hand, they find that the IMR, within  $1.7'$  from the centre, has everywhere  $\sigma \gtrsim 14 \text{ km s}^{-1}$ , significantly higher than what was found here and elsewhere at outer radii ( $\sigma \lesssim 11 \text{ km s}^{-1}$ ; Bellazzini et al. 2008; Carlberg & Grillmair 2022; M13), possibly indicating a local deepening of the potential well in the innermost nuclear regions (see also Ibata et al. 2009).

We used the MCMC also to explore the proper motion distributions of the MR and MP sub-samples, taking into account the uncertainties and the correlations between the two components of the individual *Gaia* measures ( $\text{pmra\_pmdec\_corr}$ ). In this case, the underlying model is a 2D Gaussian distribution with five parameters:  $\langle \text{pmra} \rangle$ ,  $\langle \text{pmdec} \rangle$ ,  $\sigma_{\text{int}}^{\text{pmra}}$ ,  $\sigma_{\text{int}}^{\text{pmdec}}$ , and  $\rho$ , where  $\rho$  is the correlation coefficient. Uniform priors were adopted for all the parameters, informed on the literature (Gaia Collaboration 2018b; Vasiliev & Belokurov 2020): The means were set to range between  $-5.0 \text{ mas yr}^{-1}$  and  $0.0 \text{ mas yr}^{-1}$ , the intrinsic dispersions between  $0.0 \text{ mas yr}^{-1}$  and  $0.5 \text{ mas yr}^{-1}$ , and  $\rho$  between  $-1.0$  and  $1.0$ . The posterior PDF was sampled with 30 independent MCMCs of 6000 steps each after a burn-in phase of 1000 steps for each chain. The main results of this analysis are summarised in Table 2 and presented in Fig. 10. The MP component displays significantly higher values of the velocity dispersion than the MR component in both components of the motion in the plane of the sky, thus mirroring the result form for the RV distributions. Moreover, while the correlation is compatible with zero for MP stars, it is significantly larger than zero ( $\geq 3\sigma$ ) in the MR sub-sample, possibly indicating faster rotation of the MR component also in the plane of the sky.

In conclusion, our analysis strongly supports the hypothesis that the chemo-dynamics differences observed in the Sgr Stream originated in the progenitor and are still imprinted on the kinematics of the present-day main body. Our results are purely differential, are limited to a small radial range, and to the line-of-sight velocity. They show a non-rotating and

dynamically hot MP component and a colder but weakly rotating MR component, which might intriguingly indicate a (thick, Sánchez-Janssen et al. 2010) disc + halo structure of the original Sgr progenitor (see also Mayer et al. 2001; Kazantzidis et al. 2011; del Pino et al. 2021; Carlberg & Grillmair 2022). A rotating progenitor may help to explain the observed bifurcation of the stream (Peñarrubia et al. 2010; Oria et al. 2022; Carlberg & Grillmair 2022).

## 6. Summary and conclusion

We have presented the results of a spectroscopic study aimed at obtaining the metallicity distribution in the core of the Sgr dSph, outside of the nuclear region ( $88 \text{ pc} \lesssim R \lesssim 277 \text{ pc}$ ). The sample of RGB stars was carefully selected to avoid any metallicity bias. The adopted selection technique resulted in a 100% efficiency in identifying bona fide Sgr members, as the membership of all 450 observed stars was confirmed with RV.

The MDF we derived is characterised by a strong metal-rich peak at  $[\text{Fe}/\text{H}] \approx -0.5$  plus a wide and weak tail reaching  $[\text{Fe}/\text{H}] \leq -2.0$ . According to a Gaussian mixture model analysis, the MD is best reproduced by two Gaussian distributions with a mean and standard deviation  $(\mu_1, \sigma_{1,\text{int}}) = (-0.48, 0.11)$  and  $(\mu_2, \sigma_{2,\text{int}}) = (-1.08, 0.37)$ , respectively. The first component accounts for  $\approx 75\%$  of the entire sample. Physically motivated chemical evolution models reproducing the observed abundance pattern of Sgr dSph (M17) are unable to adequately describe the observed MDF without assuming the removal of a significant fraction of metal-poor stars through the selective tidal stripping that has been invoked to explain the metallicity gradient along the Sgr stream (Law & Majewski 2016; Gibbons et al. 2017; Johnson et al. 2020, and references therein).

The most recent MDFs from large APOGEE samples (Hayes et al. 2020; Hasselquist et al. 2021) compare reasonably well with ours, showing that they are only mildly affected by metallicity biases. However, we showed that all stars more metal-poor than  $[\text{Fe}/\text{H}] = -1.0$  are slightly under-represented in these samples with respect to ours.

We confirm an earlier result by M13 of a correlation between the chemical abundance and the kinematic properties of the Sgr dSph stars. In particular, we find that the RV distribution of stars with  $[\text{Fe}/\text{H}] \geq -0.6$  clearly favours lower values of the velocity dispersion and higher values of rotation velocity than those found for the complementary metal-poor sub-sample ( $[\text{Fe}/\text{H}] < -0.6$ ). The MP population displays a significantly higher velocity dispersion than the MR population in each component of the motion in the plane of the sky as well. This result mirrors recent findings concerning samples in the Sgr stream (Gibbons et al. 2017, in particular), suggesting that the progenitor of Sgr may have hosted a more compact metal-rich discy component surrounded by a dynamically hotter and more extended metal-poor halo.

The results presented here provide an independent assessment of and a deeper insight into the chemo-dynamical properties of the stars in the core of the Sgr dSph galaxy. This is a further step toward the full characterisation of this exceedingly interesting and complex system.

*Acknowledgements.* The data presented and analysed in this paper were collected under the ESO program 105.20AH.001. MB acknowledges the financial support to this research by the PRIN-INAF Grant 1.05.01.85.14 Building up the halo: chemo-dynamical tagging in the age of large surveys (P.I. Sara Lucatello). This work has made use of data from the European Space Agency (ESA) mission *Gaia* (<https://www.cosmos.esa.int/gaia>), processed by

the *Gaia* Data Processing and Analysis Consortium (DPAC, <https://www.cosmos.esa.int/web/gaia/dpac/consortium>). Funding for the DPAC has been provided by national institutions, in particular the institutions participating in the *Gaia* Multilateral Agreement. This work has made use of Sloan Digital Sky Survey IV (SDSS-IV) data. Funding for the SDSS-IV has been provided by the Alfred P. Sloan Foundation, the U.S. Department of Energy Office of Science, and the Participating Institutions. SDSS-IV acknowledges support and resources from the Center for High-Performance Computing at the University of Utah. The SDSS website is [www.sdss.org](http://www.sdss.org). SDSS-IV is managed by the Astrophysical Research Consortium for the Participating Institutions of the SDSS Collaboration including the Brazilian Participation Group, the Carnegie Institution for Science, Carnegie Mellon University, the Chilean Participation Group, the French Participation Group, Harvard-Smithsonian Center for Astrophysics, Instituto de Astrofísica de Canarias, The Johns Hopkins University, Kavli Institute for the Physics and Mathematics of the Universe (IPMU)/University of Tokyo, the Korean Participation Group, Lawrence Berkeley National Laboratory, Leibniz Institut für Astrophysik Potsdam (AIP), Max-Planck-Institut für Astronomie (MPIA Heidelberg), Max-Planck-Institut für Astrophysik (MPA Garching), Max-Planck-Institut für Extraterrestrische Physik (MPE), National Astronomical Observatories of China, New Mexico State University, New York University, University of Notre Dame, Observatório Nacional/MCTI, The Ohio State University, Pennsylvania State University, Shanghai Astronomical Observatory, United Kingdom Participation Group, Universidad Nacional Autónoma de México, University of Arizona, University of Colorado Boulder, University of Oxford, University of Portsmouth, University of Utah, University of Virginia, University of Washington, University of Wisconsin, Vanderbilt University, and Yale University.

## References

- Abdurro'uf, Accetta, K., Aerts, C., et al. 2022, *ApJS*, 259, 35  
 Alard, C. 2001, *A&A*, 377, 389  
 Alfaro-Cuello, M., Kacharov, N., Neumayer, N., et al. 2019, *ApJ*, 886, 57  
 Alfaro-Cuello, M., Kacharov, N., Neumayer, N., et al. 2020, *ApJ*, 892, 20  
 Antoja, T., Ramos, P., Mateu, C., et al. 2020, *A&A*, 635, L3  
 Battaglia, G., & Nipoti, C. 2022, *Nat. Astron.*, 6, 659  
 Battaglia, G., Tolstoy, E., Helmi, A., et al. 2006, *A&A*, 459, 423  
 Bellazzini, M., Ferraro, F. R., & Buonanno, R. 1999, *MNRAS*, 304, 633  
 Bellazzini, M., Newberg, H. J., Correnti, M., Ferraro, F. R., & Monaco, L. 2006, *A&A*, 457, L21  
 Bellazzini, M., Ibata, R. A., Chapman, S. C., et al. 2008, *AJ*, 136, 1147  
 Bellazzini, M., Ibata, R., Malhan, K., et al. 2020, *A&A*, 636, A107  
 Carlberg, R. G., & Grillmair, C. J. 2022, *ApJ*, 935, 14  
 Carlin, J. L., Majewski, S. R., Casetti-Dinescu, D. I., et al. 2012, *ApJ*, 744, 25  
 Carlin, J. L., Sheffield, A. A., Cunha, K., & Smith, V. V. 2018, *ApJ*, 859, L10  
 Carr, C., Johnston, K. V., Laporte, C. F. P., & Ness, M. K. 2022, *MNRAS*, 516, 5067  
 Carretta, E., Bragaglia, A., Gratton, R. G., et al. 2009, *A&A*, 505, 117  
 Carretta, E., Bragaglia, A., Gratton, R. G., et al. 2010a, *A&A*, 520, A95  
 Carretta, E., Bragaglia, A., Gratton, R. G., et al. 2010b, *ApJ*, 714, L7  
 Chou, M.-Y., Majewski, S. R., Cunha, K., et al. 2007, *ApJ*, 670, 346  
 Cirasuolo, M., Fairley, A., Rees, P., et al. 2020, *The Messenger*, 180, 10  
 de Boer, T. J. L., Belokurov, V., Beers, T. C., & Lee, Y. S. 2014, *MNRAS*, 443, 658  
 del Pino, A., Fardal, M. A., van der Marel, R. P., et al. 2021, *ApJ*, 908, 244  
 Dierickx, M. I. P., & Loeb, A. 2017, *ApJ*, 847, 42  
 Evans, D. W., Riello, M., De Angeli, F., et al. 2018, *A&A*, 616, A4  
 Ferguson, P. S., & Strigari, L. E. 2020, *MNRAS*, 495, 4124  
 Gaia Collaboration (Brown, A. G. A., et al.) 2018a, *A&A*, 616, A1  
 Gaia Collaboration (Helmi, A., et al.) 2018b, *A&A*, 616, A12  
 Gaia Collaboration (Brown, A. G. A., et al.) 2021, *A&A*, 650, C3  
 Gibbons, S. L. J., Belokurov, V., & Evans, N. W. 2017, *MNRAS*, 464, 794  
 Gonzalez, O. A., Mucciarelli, A., Origlia, L., et al. 2020, *The Messenger*, 180, 18  
 Harbeck, D., Grebel, E. K., Holtzman, J., et al. 2001, *AJ*, 122, 3092  
 Harris, W. E. 1996, *AJ*, 112, 1487  
 Hasselquist, S., Shetrone, M., Smith, V., et al. 2017, *ApJ*, 845, 162  
 Hasselquist, S., Carlin, J. L., Holtzman, J. A., et al. 2019, *ApJ*, 872, 58  
 Hasselquist, S., Hayes, C. R., Lian, J., et al. 2021, *ApJ*, 923, 172  
 Hayes, C. R., Majewski, S. R., Hasselquist, S., et al. 2020, *ApJ*, 889, 63  
 Huxor, A. P., & Grebel, E. K. 2015, *MNRAS*, 453, 2653  
 Ibata, R. A., Gilmore, G., & Irwin, M. J. 1994, *Nature*, 370, 194  
 Ibata, R. A., Wyse, R. F. G., Gilmore, G., Irwin, M. J., & Suntzeff, N. B. 1997, *AJ*, 113, 634  
 Ibata, R., Bellazzini, M., Chapman, S. C., et al. 2009, *ApJ*, 699, L169  
 Ibata, R., Bellazzini, M., Thomas, G., et al. 2020, *ApJ*, 891, L19  
 Johnson, B. D., Conroy, C., Naidu, R. P., et al. 2020, *ApJ*, 900, 103

- Kamann, S., Husser, T. O., Dreizler, S., et al. 2018, *MNRAS*, **473**, 5591
- Kazantzidis, S., Łokas, E. L., Callegari, S., Mayer, L., & Moustakas, L. A. 2011, *ApJ*, **726**, 98
- Kurucz, R. L. 1993, *VizieR Online Data Catalog: VI/039*
- Kurucz, R. L. 2005, *Mem. Soc. Astron. Ital.*, **8**, 14
- Laporte, C. F. P., Minchev, I., Johnston, K. V., & Gómez, F. A. 2019, *MNRAS*, **485**, 3134
- Law, D. R., & Majewski, S. R. 2010, *ApJ*, **714**, 229
- Law, D. R., & Majewski, S. R. 2016, in *Tidal Streams in the Local Group and Beyond*, eds. H. J. Newberg, & J. L. Carlin, *Astrophys. Space Sci. Lib.*, **420**, 31
- Lindegren, L., Hernández, J., Bombrun, A., et al. 2018, *A&A*, **616**, A2
- Łokas, E. L., Kazantzidis, S., Majewski, S. R., et al. 2010, *ApJ*, **725**, 1516
- Lombardo, L., François, P., Bonifacio, P., et al. 2021, *A&A*, **656**, A155
- Majewski, S. R., Skrutskie, M. F., Weinberg, M. D., & Ostheimer, J. C. 2003, *ApJ*, **599**, 1082
- Majewski, S. R., Hasselquist, S., Łokas, E. L., et al. 2013, *ApJ*, **777**, L13
- Majewski, S. R., Schiavon, R. P., Frinchaboy, P. M., et al. 2017, *AJ*, **154**, 94
- Mayer, L., Governato, F., Colpi, M., et al. 2001, *ApJ*, **547**, L123
- McConnachie, A. W. 2012, *AJ*, **144**, 4
- Minelli, A., Mucciarelli, A., Romano, D., et al. 2021, *ApJ*, **910**, 114
- Monaco, L., Ferraro, F. R., & Pancino, E. 2003, *ApJ*, **597**, L25
- Monaco, L., Bellazzini, M., Ferraro, F. R., & Pancino, E. 2004, *MNRAS*, **353**, 874
- Monaco, L., Bellazzini, M., Bonifacio, P., et al. 2005, *A&A*, **441**, 141
- Monaco, L., Bellazzini, M., Bonifacio, P., et al. 2007, *A&A*, **464**, 201
- Mucciarelli, A., & Bonifacio, P. 2020, *A&A*, **640**, A87
- Mucciarelli, A., Bellazzini, M., Ibata, R., et al. 2017, *A&A*, **605**, A46
- Mucciarelli, A., Bellazzini, M., & Massari, D. 2021, *A&A*, **653**, A90
- Niederste-Ostholt, M., Belokurov, V., & Evans, N. W. 2012, *MNRAS*, **422**, 207
- Oria, P.-A., Ibata, R., Ramos, P., Famaey, B., & Errani, R. 2022, *ApJ*, **932**, L14
- Pasquini, L., Avila, G., Blecha, A., et al. 2002, *The Messenger*, **110**, 1
- Peñarrubia, J., Belokurov, V., Evans, N. W., et al. 2010, *MNRAS*, **408**, L26
- Pryor, C., & Meylan, G. 1993, in *Structure and Dynamics of Globular Clusters*, eds. S. G. Djorgovski, & G. Meylan, *ASP Conf. Ser.*, **50**, 357
- Ramos, P., Antoja, T., Yuan, Z., et al. 2022, *A&A*, **666**, A64
- Ramos, P., Mateu, C., Antoja, T., et al. 2020, *A&A*, **638**, A104
- Riello, M., De Angeli, F., Evans, D. W., et al. 2021, *A&A*, **649**, A3
- Romano, D., Bellazzini, M., Starkenburg, E., & Leaman, R. 2015, *MNRAS*, **446**, 4220
- Ruiz-Lara, T., Gallart, C., Bernard, E. J., & Cassisi, S. 2020, in *XIV.0 Scientific Meeting (virtual) of the Spanish Astronomical Society*, 185
- Sánchez-Janssen, R., Méndez-Abreu, J., & Aguerri, J. A. L. 2010, *MNRAS*, **406**, L65
- Schlafly, E. F., & Finkbeiner, D. P. 2011, *ApJ*, **737**, 103
- Schlegel, D. J., Finkbeiner, D. P., & Davis, M. 1998, *ApJ*, **500**, 525
- Scrucca, L., Fop, M., Murphy, T. B., & Raftery, A. E. 2016, *The R Journal*, **8**, 289
- Siegel, M. H., Dotter, A., Majewski, S. R., et al. 2007, *ApJ*, **667**, L57
- Stetson, P. B., & Pancino, E. 2008, *PASP*, **120**, 1332
- Taibi, S., Battaglia, G., Leaman, R., et al. 2022, *A&A*, **665**, A92
- Tolstoy, E., Irwin, M. J., Helmi, A., et al. 2004, *ApJ*, **617**, L119
- Tosi, M. 1988, *A&A*, **197**, 33
- Vasiliev, E., & Belokurov, V. 2020, *MNRAS*, **497**, 4162
- Vasiliev, E., Belokurov, V., & Erkal, D. 2021, *MNRAS*, **501**, 2279
- Vitali, S., Arentsen, A., Starkenburg, E., et al. 2022, *MNRAS*, **517**, 6121
- Walker, M. G., Mateo, M., Olszewski, E. W., et al. 2006, *AJ*, **131**, 2114
- Yang, C., Xue, X.-X., Li, J., et al. 2019, *ApJ*, **886**, 154